Anisotropic hydrodynamic modeling of 200 GeV Au-Au collisions

Dekrayat Almaalol
Department of Physics, Kent State University, Kent, Ohio 44242, USA

Mubarak Alqahtani
Department of Basic Sciences, College of Education, Imam Abdulrahman Bin Faisal University, Dammam 34212, Saudi Arabia

Michael Strickland
Department of Physics, Kent State University, Kent, Ohio 44242, USA

(Received 26 July 2018; revised manuscript received 26 December 2018; published 3 April 2019)

We compare phenomenological results from $(3+1)$-dimensional quasiparticle anisotropic hydrodynamics (aHydroQP) with experimental data collected from RHIC 200 GeV Au-Au collisions. We compare identified particle spectra in different centrality classes, charged particle multiplicity versus pseudorapidity, identified particle multiplicity versus centrality across a wide range of particle species, identified particle elliptic flow versus transverse momentum, and charged particle elliptic flow as a function of transverse momentum and rapidity. We use the same aHydroQP and hadronic production codes that were used previously to describe LHC 2.76 TeV data. The aHydroQP hydrodynamic model includes the effects of both shear and bulk viscosities in addition to an infinite number of transport coefficients computed self-consistently in the relaxation-time approximation. To convert to the final-state hadrons, we use anisotropic Cooper–Frye freeze-out performed on a fixed-energy-density hypersurface and compute the production and feed-down by using a customized version of Therminator 2. We find good agreement with many heavy-ion collision observables using only smooth Glauber initial conditions parametrized by an initial central temperature of $T_0 = 455$ MeV, a constant shear-viscosity-to-entropy-density ratio $\eta/s = 0.179$, and a switching (freeze-out) temperature of $T_{\rm FO} = 130$ MeV.

DOI: 10.1103/PhysRevC.99.044902

I. INTRODUCTION

Ultrarelativistic heavy-ion collisions (URHICs) performed at the Relativistic Heavy Ion Collider (RHIC) at Brookhaven National Laboratory and the Large Hadron Collider (LHC) at CERN aim to create and study the properties of a deconfined quark-gluon plasma (QGP). At zero baryochemical potential, the QGP is expected to be generated when temperatures exceed approximately 155 MeV. In the QGP phase, quarks and gluons, which are liberated from incoming nuclei, are the relevant degrees of freedom. In the high-energy limit, color transparency results in the central rapidity region of the matter generated in such collisions having net baryon number close to zero, which mimics conditions generated in the early universe. However, the lifetime of the QGP created in URHICs is on the order of 10 fm/c, which begs the question of whether the matter generated can be described by using models which assume that the system is in local isotropic thermal equilibrium. The ability of ideal hydrodynamics to qualitatively describe soft hadron production and flow [1–3] led to early claims that the QGP was isotropic and thermal on a timescale on the order of 0.5 fm/c (see, e.g., Refs. [4–9]).

We now know that this claim was premature and that the QGP generated in URHICs is most likely momentum-space anisotropic in the local rest frame (LRF) of the matter, with the anisotropies being largest at early times $\tau \lesssim 2$ fm/c and near the edges of the QGP at all times [10–12]. Traditionally, the existence of LRF momentum-space anisotropies is accounted for in the context of second-order viscous hydrodynamics by formally expanding in a gradient expansion around a locally isotropic and thermal state. Early work along these lines was presented in a series of papers by Mueller, Israel, and Stewart (MIS) decades ago [13–15]. The success of viscous relativistic hydrodynamics resulted in many works which have improved upon the MIS formalism, and the resulting improved second-order hydrodynamical models have had great phenomenological success in describing a host of URHIC data [16–47]. Currently, there is a concerted effort to quantitatively extract QGP properties such as the average initial central temperature of the QGP, its shear viscosity, its bulk viscosity, jet energy loss, the heavy quark momentum diffusion constant, etc. For recent reviews of relativistic hydrodynamics in the context of the QGP, we refer the reader to Refs. [48–50].

In parallel to these developments in second-order viscous hydrodynamics theory and phenomenology, there have been theoretical and phenomenological works dedicated to relaxing the assumption that the QGP is close to local isotropic thermal equilibrium in order to better account for large deviations from isotropy. To address this issue, a framework called anisotropic hydrodynamics (aHydro) was introduced [51,52]. This framework allows one to describe a system that is far from equilibrium (isotropy) without breaking important physics constraints such as the positivity of the one-particle distribution function, etc. In all cases where exact solutions to

the Boltzmann equation are available, it has been found that aHydroQP provides a much better approximation to the exact solutions than standard second-order schemes, particularly when the system is far from equilibrium [53–61].

There has been a significant body of work produced since the two early aHydro papers [51,52], which has extended the aHydro formalism to full $(3+1)$-dimensional [$(3+1)$d] dynamics, self-consistent inclusion of nonconformality of the QGP using a quasiparticle framework, etc. [56,60,62–79]. For a recent aHydro review, we refer the reader to Ref. [12]. In this paper, we use quasiparticle aHydro (aHydroQP), which implements the QCD equation of state via a temperature-dependent quasiparticle mass that is fit to lattice data for the entropy density [71]. The aHydroQP formalism has been previously applied to LHC 2.76 TeV collisions and it was demonstrated that one could reproduce the observed identified particle differential spectra, charged particle multiplicity, elliptic flow, and Hanbury-Brown–Twiss radii [76,77]. By using smooth Glauber initial conditions, the extracted initial central temperature was $T_0 = 600$ MeV at $\tau_0 = 0.25$ fm/c and the extracted shear-viscosity-to-entropy-density ratio was $\eta/s = 0.159$ with a switching (freeze-out) temperature of $T_{\rm FO} = 130$ MeV.

In this paper, we present the corresponding determination at RHIC's highest collision energy. Keeping the switching temperature fixed, since this should be independent of the collision energy, we present fits to spectra, multiplicities, etc. and extract values of η/s and T_0 for 200 GeV Au-Au collisions. Our best fits to the spectra resulted in $T_0 = 455$ MeV at $\tau_0 = 0.25$ fm/c and $\eta/s = 0.179$. With these values, we find good agreement with the available data for the identified particle spectra, elliptic flow in noncentral centrality classes, charged particle multiplicities, and identified particle multiplicities across a broad range of centrality classes. The resulting parameter set for the highest RHIC energies will be useful in other contexts where aHydro is being used for background evolution, e.g., for bottomonium-suppression calculations [80–85]. In addition, this study will serve as a baseline for future work including, e.g., varying the initial momentum-space anisotropy, fluctuating initial conditions, finite density, etc.

The structure of the paper is as follows: In Sec. II we present our setup and background for the aHydroQP calculations. In Sec. III we present our main results and compare with experimental data from PHENIX, PHOBOS, and STAR collaborations. In Sec. IV we summarize our findings and present an outlook for the future.

Conventions and notation

The Minkowski metric tensor is taken to be "mostly minus," i.e., $g^{\mu\nu} = \mathrm{diag}(+,-,-,-)$. The transverse projection operator $\Delta^{\mu\nu} = g^{\mu\nu} - u^\mu u^\nu$ is used to project four-vectors and/or tensors into the space orthogonal to u^μ. The Lorentz-invariant integration measure is $dP = \frac{d^3\mathbf{p}}{(2\pi)^3}(p\cdot u)^{-1}$.

II. SETUP AND BACKGROUND

In anisotropic hydrodynamics, we take the one-particle distribution function to be of generalized Romatschke–Strickland form [86,87]:

$$f(x,p) = f_{\rm eq}\left(\frac{1}{\lambda}\sqrt{p_\mu \Xi^{\mu\nu} p_\nu}\right), \tag{1}$$

where λ is a temperature-like scale. One can decompose the symmetric anisotropy four-tensor $\Xi^{\mu\nu} = u^\mu u^\nu + \xi^{\mu\nu} - \Delta^{\mu\nu}\Phi$, with Φ encoding bulk viscous corrections, $u_\mu \xi^{\mu\nu} = u_\nu \xi^{\mu\nu} = 0$ and $\xi^\mu{}_\mu = 0$ [56]. Taking the anisotropy tensor $\xi^{\mu\nu}$ to be diagonal, one can rewrite the distribution function in the LRF in terms of the spacelike diagonal anisotropy factors α_i:

$$f(x,p) = f_{\rm eq}\left(\frac{1}{\lambda}\sqrt{\sum_i \frac{p_i^2}{\alpha_i^2} + m^2}\right), \tag{2}$$

with $i \in \{x,y,z\}$ and $\alpha_i \equiv (1+\xi_i+\Phi)^{-1/2}$. During the evolution phase, m is a function of the local temperature and, for the purposes of freeze-out, m is the mass of the particular hadron species under consideration.

A. The quasiparticle Boltzmann equation

For a system of quasiparticles with a temperature-dependent mass $m(T)$, the Boltzmann equation is [71,88,89]

$$p^\mu \partial_\mu f + \tfrac{1}{2}\partial_i m^2 \partial^i_{(p)} f = -\mathcal{C}[f]. \tag{3}$$

The quasiparticle mass $m(T)$ is determined uniquely from the lattice entropy density. To conserve energy and guarantee thermodynamic consistency it is necessary to introduce a temperature-dependent background contribution $B(T)$ which is determined uniquely in terms of $m(T)$ and a boundary condition at $T = 0$ by using

$$\partial_\mu B = -\frac{1}{2}\partial_\mu m^2 \int dP f(x,p). \tag{4}$$

For the details of the equation of state implementation, the resulting temperature-dependent quasiparticle mass $m(T)$ and background contribution $B(T)$, and the associated bulk viscosity, we direct the reader to Refs. [71,77].

For the collisional kernel, we use the relaxation-time approximation (RTA) kernel

$$C[f] = \frac{p\cdot u}{\tau_{\rm eq}}[f - f_{\rm eq}(T)]. \tag{5}$$

The relaxation time for massive quasiparticles is

$$\tau_{\rm eq}(T) = \bar{\eta}\frac{\mathcal{E}+P}{I_{3,2}(\hat{m}_{\rm eq})}, \tag{6}$$

where $\bar{\eta} = \eta/s$ and

$$I_{3,2}(x) = \frac{N_{\rm dof} T^5 x^5}{30\pi^2}\left[\frac{1}{16}[K_5(x) - 7K_3(x) + 22K_1(x)] - K_{i,1}(x)\right],$$
$$K_{i,1}(x) = \frac{\pi}{2}[1 - xK_0(x)\mathcal{S}_{-1}(x) - xK_1(x)\mathcal{S}_0(x)], \tag{7}$$

where $N_{\rm dof}$ is the number of degrees of freedom, K_n are modified Bessel functions of the second kind, and $\mathcal{S}_n$ are modified Struve functions [71].

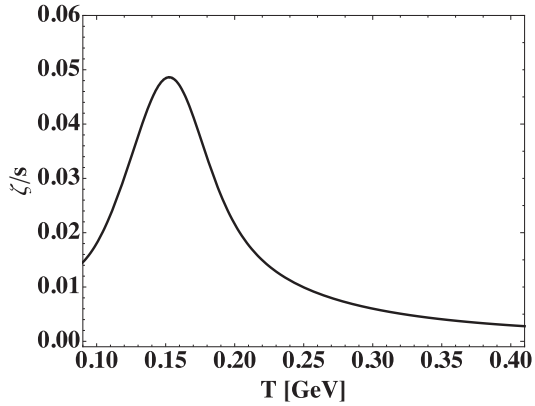

FIG. 1. Quasiparticle model bulk viscosity over entropy density as a function of temperature.

Once $\tau_{\rm eq}$ is fixed in terms of $\bar{\eta}$ one can calculate the bulk viscosity of the system [12]. In Fig. 1, we plot the resulting bulk-viscosity-to-entropy-density ratio ζ/s as a function of temperature. As can be seen from this figure, the quasiparticle model used predicts that the magnitude of ζ/s peaks at approximately 0.05 at a temperature of approximately 155 MeV. This temperature dependence and magnitude are consistent with results from a phenomenological extraction using Bayesian techniques [90] and nonconformal AdS/CFT models [91], however, it is much lower in magnitude than that found in Ref. [92].

B. The energy-momentum tensor

The background contribution $B(T)$ is added to the kinetic-energy-momentum tensor as follows:

$$T^{\mu\nu} = T^{\mu\nu}_{\rm kinetic} + B(T)g^{\mu\nu}, \tag{8}$$

and, assuming a diagonal anisotropy tensor in the LRF, we can expand the energy-momentum tensor as

$$T^{\mu\nu} = \mathcal{E}u^\mu u^\nu + \mathcal{P}_x X^\mu X^\nu + \mathcal{P}_y Y^\mu Y^\nu + \mathcal{P}_z Z^\mu Z^\nu. \tag{9}$$

where u^μ is the timelike fluid velocity and X^μ, Y^μ, and Z^μ are spacelike four-vectors which span the directions orthogonal to u^μ.[1] Below we also use a compact notation $X_i^\mu = (X^\mu, Y^\mu, Z^\mu)$. The energy density and pressures appearing in Eq. (9) each include kinetic and background field contributions with $B(T)$ adding to the kinetic-energy density and subtracting from each of the kinetic pressures isotropically.

C. Equations of motion

To obtain the equations of motion, we take moments of the Boltzmann equation using an integral operator of the form $\hat{\mathcal{O}}^{\mu\nu\cdots\lambda} = \int dP p^\mu p^\nu \cdots p^\lambda$.

[1]Details concerning the vector basis used can be found in Refs. [71,77].

1. First moment of Boltzmann equation

The first moment of the Boltzmann equation provides four equations

$$D_u\mathcal{E} + \mathcal{E}\theta_u + \sum_i \mathcal{P}_i u_\mu D_i X_i^\mu = 0,$$
$$D_i\mathcal{P}_i + \mathcal{P}_i\theta_i - \mathcal{E}X^i_\mu D_u u^\mu - \sum_j \mathcal{P}_j X^i_\mu D_j X_j^\mu = 0, \tag{10}$$

where $i \in \{x, y, z\}$ and $j = \{x, y, z\}\backslash\{i\}$. For example, for $i = x$, $j \in \{y, z\}$. Above, D_u is the comoving derivative along the direction of the fluid velocity, $D_u = u^\mu\partial_\mu$. Likewise, $D_i = X_i^\mu\partial_\mu$.

2. Second moment of Boltzmann equation

For the second moment we encounter the rank-three tensor

$$\mathcal{I}^{\mu\nu\lambda} \equiv \int dP p^\mu p^\nu p^\lambda f(x, p), \tag{11}$$

which can be expanded in the vector basis as

$$\mathcal{I}^{\mu\nu\lambda} = \mathcal{I}_u u^\mu u^\nu u^\lambda + \sum_i \mathcal{I}_i\left[u^\mu X_i^\nu X_i^\lambda + X_i^\mu u^\nu X_i^\lambda + X_i^\mu X_i^\nu u^\lambda\right], \tag{12}$$

with $i \in \{x, y, z\}$ and

$$\mathcal{I}_i = \alpha\alpha_i^2\mathcal{I}_{\rm eq}(\lambda, m), \quad \mathcal{I}_{\rm eq}(\lambda, m) = 4\pi\tilde{N}\lambda^5\hat{m}^3K_3(\hat{m}), \tag{13}$$

where $\alpha = \prod_i \alpha_i$, $\hat{m} = m/\lambda$, and $\tilde{N} = N_{\rm dof}/(2\pi)^3$ [56].

We obtain three equations of motion from the diagonal projections of the second moment of the Boltzmann equation by using $X_\mu X_\nu\partial_\alpha\mathcal{I}^{\alpha\mu\nu}$, $Y_\mu Y_\nu\partial_\alpha\mathcal{I}^{\alpha\mu\nu}$, and $Z_\mu Z_\nu\partial_\alpha\mathcal{I}^{\alpha\mu\nu}$ giving [71]

$$D_u\mathcal{I}_i + \mathcal{I}_i\left(\theta_u + 2u_\mu D_i X_i^\mu\right) = \frac{1}{\tau_{\rm eq}}[\mathcal{I}_{\rm eq}(T, m) - \mathcal{I}_i], \tag{14}$$

where, once again, $i \in \{x, y, z\}$.

3. Effective temperature

In the above equations we have eight unknowns u_i, α_i, λ, and T and seven equations (four from the first moment and three from the second moment). To close the equations we obtain the effective temperature T from the nonequilibrium energy density, $\mathcal{E}(\boldsymbol{\alpha}, \lambda, m) = \mathcal{E}_{\rm eq}(T)$. This is referred to as the matching condition. In the RTA, this matching condition is a direct consequence of enforcing energy-momentum conservation. The resulting matching condition is

$$\mathcal{H}_3(\boldsymbol{\alpha}, \hat{m})\lambda^4 = \mathcal{H}_{3,\rm eq}(1, \hat{m}_{\rm eq})T^4, \tag{15}$$

with $\hat{m}_{\rm eq} = m/T$. The function $\mathcal{H}_3$ and its efficient evaluation are described in Appendix B of Ref. [77].

D. Freeze-out prescription

To convert from a fluid description to a particle description, we use the same form for the one-particle distribution function (2) as used in the evolution. We first extract a fixed energy density hypersurface corresponding to an effective temperature of $T_{\rm FO} = 130$ MeV and extract the microscopic parameters $(\boldsymbol{\alpha}_i, \lambda, \mathbf{u})$ on the hypersurface. We then loop over 370 hadrons

and hadron resonances indexed by i and integrate over the hypersurface

$$\left(p^0\frac{dN}{d^3p}\right)_i = \frac{\mathcal{N}_i}{(2\pi)^3}\int f_i(x,p)p^\mu d^3\Sigma_\mu \tag{16}$$

to extract the hadronic spectra. Above, the mass in the distribution function is the mass of the ith hadron and $\mathcal{N}_i$ counts the number of internal degrees of freedom (spin, etc.) for hadron species i. For details on the hypersurface parametrization used and other details, we refer the reader to Sec. VI of Ref. [93]. The resulting parametrized hypersurface and microscopic variables are then exported in a format suitable for use by Therminator 2 [94]. We produced a customized version of Therminator 2 which allows for an ellipsoidally deformed distribution function on the freeze-out hypersurface. This customized version takes care of all hadronic production, decays, and resonance feed-downs. The $(3+1)$d aHydroQP code and the customized version of Therminator 2 are both available publicly by using the URL found in Ref. [95].

In this context, we should mention that the freeze-out prescription outlined above only matches the "kinetic" contribution to the energy-momentum tensor and discards the background contribution B at freeze-out. To incorporate this contribution self-consistently one would have to freeze-out to a hadron resonance gas model which also includes a background (mean field) term. As such, we currently ignore this contribution to the energy-momentum tensor. One can estimate the size of this background field contribution by comparing the relative contribution of B to the total energy density at $T_{\rm FO} = 130$ MeV. Computing $B_{\rm eq}/\mathcal{E}_{\rm eq}$ at $T_{\rm FO}$ one finds that B contributes approximately 2.8% to the energy density.[2]

Finally, we should also discuss the degree to which our quasiparticle EoS reproduces the equation of state of a noninteracting hadron gas at freeze-out. For this purpose we summed over 370 hadrons from the Particle Data Group listings, taking into account the appropriate quantum statistics for each particle. We find that at $T = 130$ MeV, the quasiparticle EoS energy density is -2.5% different than the hadron resonance gas result and the pressure is -9.4% different. As a result, we only conserve energy to within 2.5% at freeze-out coming from a slight mismatch between our EoS and a free hadron gas.

III. RESULTS

We now turn to our phenomenological results. We consider $\sqrt{s_{\rm NN}} = 200$ GeV Au-Au collisions and compare with data from the PHENIX, STAR, and PHOBOS collaborations. In all results presented herein, we used our customized version of Therminator 2 to Monte Carlo sample production and decays based on the freeze-out hypersurface and microscopic parameters provided by aHydroQP. Depending on the observable and the centrality class considered, we used between 10 500 and 100 500 Monte Carlo sampled hadronic production and decay events. In all plots, the shaded bands surrounding the theory results indicate the statistical uncertainty associated with the hadronic production and decay sampling.

A. Initial conditions

For the initial conditions, we assume the system to be initially isotropic in momentum space $[\alpha_i(\tau_0) = 1]$, with zero transverse flow $[\mathbf{u}_\perp(\tau_0) = 0]$ and Bjorken flow in the longitudinal direction $[\vartheta(\tau_0) = \eta]$. In the transverse plane, the initial energy density distribution is obtained from a "tilted" Glauber profile [96]. The profile function used was a linear combination of smooth Glauber wounded-nucleon and binary-collision density profiles, with a binary-collision mixing factor of $\chi = 0.145$. In the rapidity direction, we used a profile with a central plateau and Gaussian "tails" in the fragmentation region

$$\rho(\varsigma) \equiv \exp\big[-(\varsigma-\Delta\varsigma)^2/\big(2\sigma_\varsigma^2\big)\Theta(|\varsigma|-\Delta\varsigma)\big]. \tag{17}$$

The parameters entering Eq. (17) were fit to the observed pseudorapidity distribution of charged hadrons, with the results being $\Delta\varsigma = 1.4$ and $\sigma_\varsigma = 1.4$. The variable $\Delta\varsigma$ sets the initial width of the central plateau and the variable σ_ς sets the initial width of the fragmentation Gaussians.

The resulting initial energy density at a given transverse position $\mathbf{x}_\perp$ and spatial rapidity ς was computed by using

$$\begin{aligned}\mathcal{E}(\mathbf{x}_\perp,\varsigma) \propto{}& (1-\chi)\rho(\varsigma)[W_A(\mathbf{x}_\perp)g(\varsigma)+W_B(\mathbf{x}_\perp)g(-\varsigma)]\\ &+\chi\rho(\varsigma)C(\mathbf{x}_\perp),\end{aligned} \tag{18}$$

where $W_{A,B}(\mathbf{x}_\perp)$ is the wounded nucleon density for nucleus A or B, $C(\mathbf{x}_\perp)$ is the binary collision density, and $g(\varsigma)$ is the tilt function. The tilt function is defined through

$$g(\varsigma) = \begin{cases} 0 & \text{if } \varsigma < -y_N \\ (\varsigma+y_N)/(2y_N) & \text{if } -y_N \leqslant \varsigma \leqslant y_N \\ 1 & \text{if } \varsigma > y_N, \end{cases} \tag{19}$$

where $y_N = \log[2\sqrt{s_{NN}}/(m_p+m_n)]$ the nucleon momentum rapidity [96].

B. Particle spectra and multiplicities

Based on our earlier study of 2.76 TeV collisions at the LHC [77], we fix the switching (freeze-out) temperature to be $T_{\rm FO} = 130$ MeV. This leaves the shear-viscosity-to-entropy-density ratio $\bar{\eta} = \eta/s$ and initial central temperature T_0 (center of the system for a $b = 0$ collision) as independent parameters. As done is our prior works, we assume that $\bar{\eta}$ is independent of the temperature. To fit T_0 and $\bar{\eta}$, we compared model predictions with the observed pion, proton, and kaon spectra in the 0%–5% and 30%–40% centrality classes. Based on these comparisons, we obtained $T_0 = 455$ MeV at $\tau_0 = 0.25$ fm/c and $\bar{\eta} = 0.179$. The resulting fits to the pion, kaon, and proton spectra are shown in Fig. 2 and compared with experimental data from the PHENIX collaboration [97]. As can be seen from this figure, the model provides a good description of the identified particle spectra with this parameter set. In high-centrality classes, we see that the model

[2]A similar computation using the evolved nonequilibrium B confirms this number.

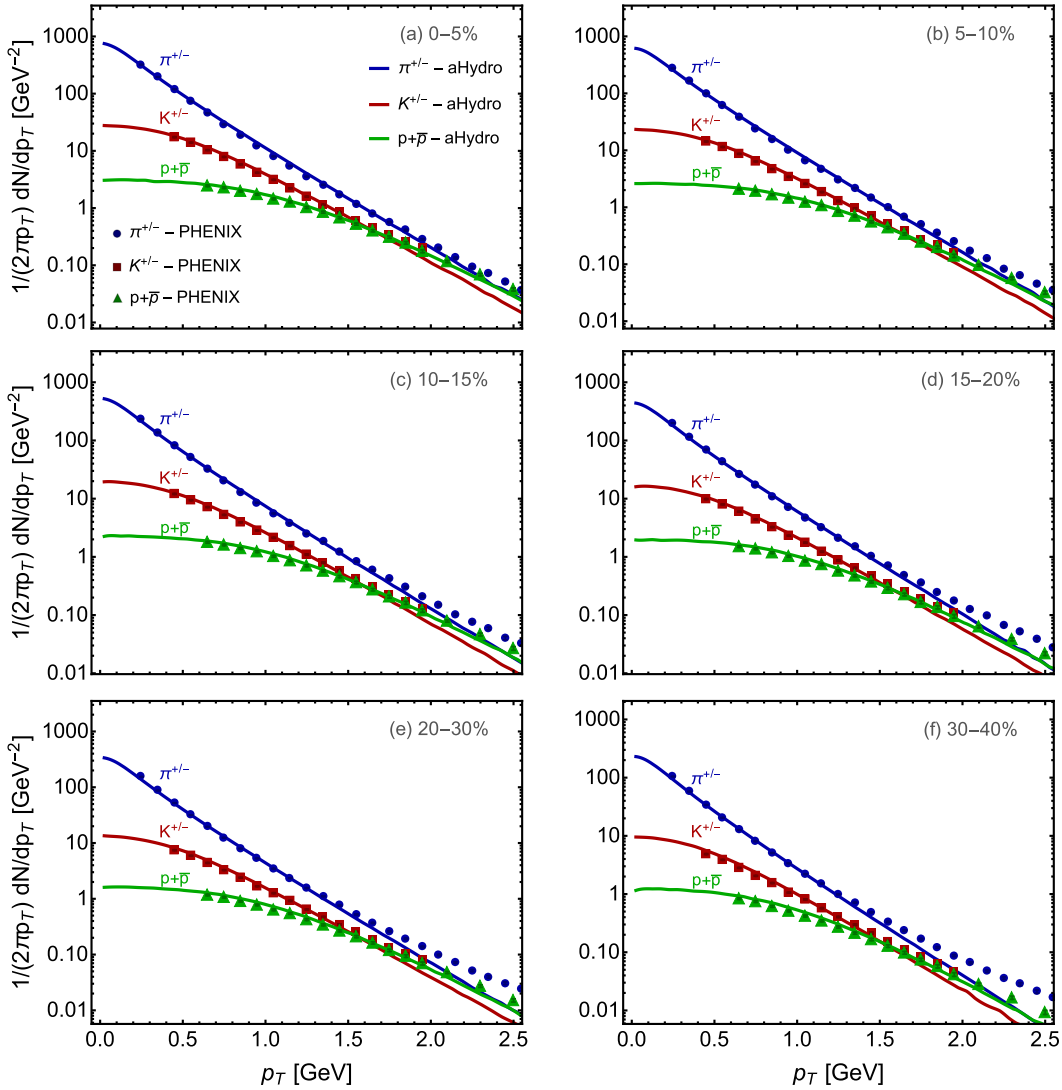

FIG. 2. Pion, kaon, and proton spectra compared with experimental observations by the PHENIX collaboration [97]. The panels show the centrality classes (a) 0%–5%, (b) 5%–10%, (c) 10%–15%, (d) 15%–20%, (e) 20%–30%, and (f) 30%–40%.

underestimates hadron production at large transverse momentum, $p_T \gtrsim 1.5$ GeV.

While the agreement with the identified particle spectra is not perfect, it is better than what has been achieved in the past by using past standard vHydro and aHydro results obtained by using the same initial conditions. The reasons for this are most likely twofold: (1) the inclusion of the bulk viscous corrections to the evolution and freeze-out distribution function and (2) the anisotropic freeze-out procedure which does not linearize around an isotropic equilibrium background. To assess the impact of the anisotropic (viscous) corrections to the identified particle spectra one can recompute hadron production by assuming an isotropic distribution function that uses only the local effective temperature as input and take the difference of the spectra obtained this way with the spectra obtained by using the full aHydroQP distribution function. To quantify this we introduce

$$\Delta \equiv \left[\left(\frac{dN}{dp_T}\right)_{\mathrm{aniso}} - \left(\frac{dN}{dp_T}\right)_{\mathrm{iso}}\right] \Big/ \left(\frac{dN}{dp_T}\right)_{\mathrm{iso}}. \qquad (20)$$

This quantity is plotted in Fig. 3 for the 0%–5% and 20%–30% centrality classes. As one can see from Fig. 3 there is a sizable correction coming from the viscous δf which seems to grow larger as the mass of the particle increases. From this result we learn that the integrated effect of the viscous correction on the particle spectra in both the 0%–5% and 20%–30% central classes is as large as 50%–100% depending on the p_T and particle species considered. We note that the magnitude of the relative correction is roughly the same in both centrality classes and that the different particle species level corrections are also similar. Additionally, we note that we repeated this exercise in all centrality classes and found similar results.

In Fig. 4 we present our results for the identified particle multiplicities as a function of centrality. From top to bottom, the particles shown are π^+, K^+, p, ϕ, and $\Omega^+ + \Omega^-$. The data for π^+, K^+, and p are from the PHENIX collaboration [97]. The data for the ϕ meson are also from the PHENIX collaboration [98]. The data for $\Omega^+ + \Omega^-$ comes from the

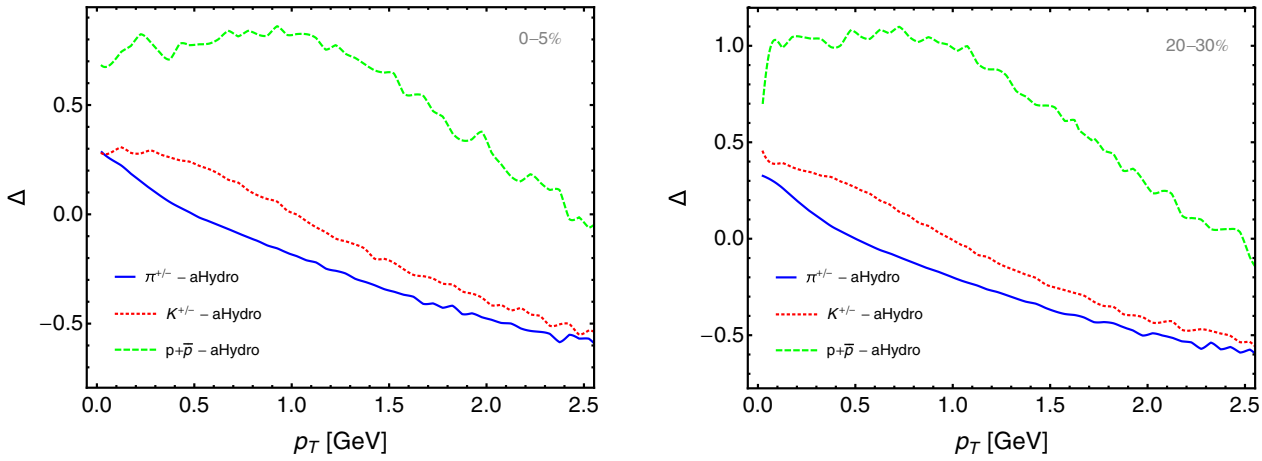

FIG. 3. (left panel) The ratio Δ defined in Eq. (20) in the 0%–5% centrality class using the full distribution (solid) and the isotropic distribution (dashed). (right panel) Same in the 20%–30% centrality class. In both panels the solid blue, dashed red, and long-dashed green lines show Δ for pions, kaons, and protons, respectively.

STAR collaboration [99]. The aHydroQP theory results are binned in the centrality bins used by PHENIX collaboration for π^+, K^+, and p. As this figure demonstrates, aHydroQP coupled to our customized version of Therminator 2 is able to reproduce the centrality dependence of the observed identified particle multiplicities quite well. This is particularly interesting because we have a single iso-thermal switching (freeze-out) temperature which is quite low, $T_{\rm FO} = 130$ MeV, and we are able to reproduce reasonably well the observed identified particle multiplicities, not only for central collisions, but across many centrality classes. That said, based on the theory-to-experiment ratios shown in Fig. 5 we see that there is an approximately 20% difference in the proton multiplicity in the 0%–5% centrality class and an approximately 35% difference in the $\Omega^+ + \Omega^-$ multiplicity in the most-central bin. These discrepancies could have their origins in the assumptions made during the aHydroQP evolution, freeze-out (single freeze-out with no chemical potentials), and/or the production and decays implemented by Therminator 2.

In Fig. 6 we present a comparison of our model predictions for the charged particle multiplicity as a function of pseudorapidity compared with experimental data from the PHOBOS collaboration [100]. In panel (a) we show centrality classes in the range 0%–25% and in panel (b) we show centrality classes in the range 25%–50%. We find that aHydroQP does a good job in reproducing the observed charged particle multiplicity as a function of pseudorapidity in a wide range of centrality classes.

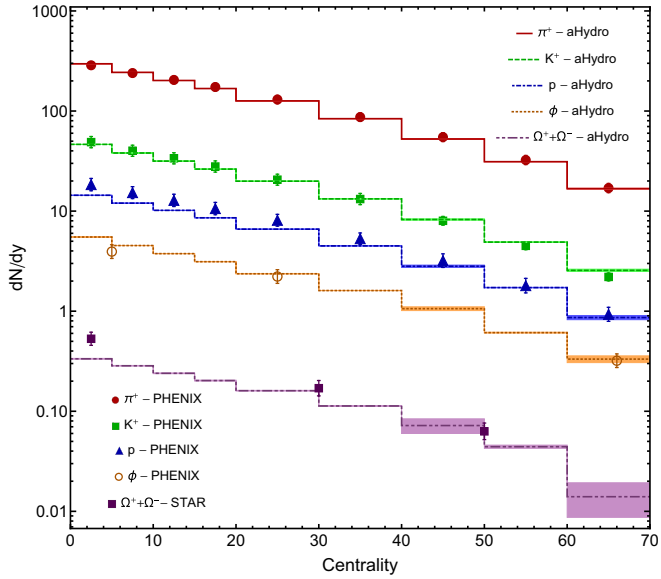

FIG. 4. Identified particle multiplicities as a function of centrality. From top to bottom, the particles shown are π^+, K^+, p, ϕ, and $\Omega^+ + \Omega^-$. The data for π^+, K^+, and p are from the PHENIX collaboration [97]. Data for the ϕ meson production are also from the PHENIX collaboration [98]. The data for $\Omega^+ + \Omega^-$ comes from the STAR collaboration [99]. The aHydroQP theory results are binned by using the centrality bins used by the PHENIX collaboration for π^+, K^+, and p.

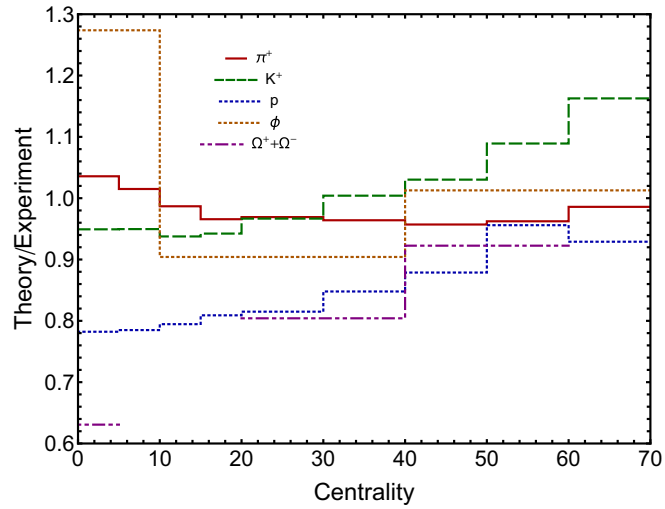

FIG. 5. Theory-to-data ratio for identified particle multiplicity (shown in Fig. 4). For this figure, we rebinned the theory predictions for the ϕ and $\Omega^+ + \Omega^-$ to match the experimental bins.

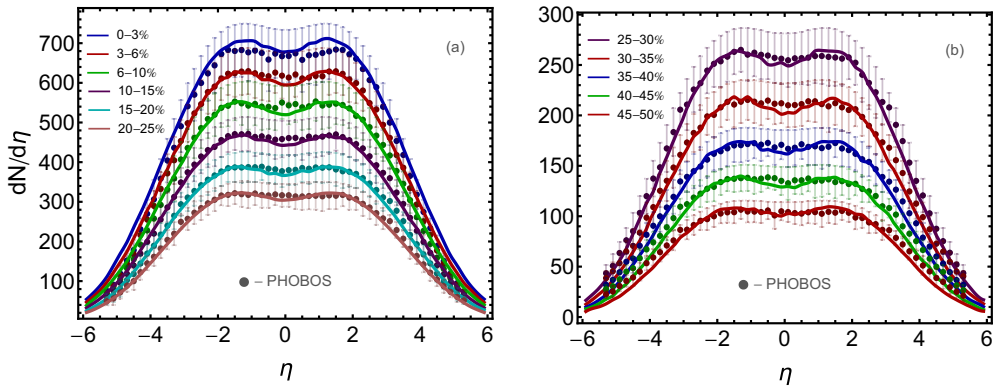

FIG. 6. aHydroQP results for charged particle multiplicity in different centrality classes (solid lines) compared with experimental data from the PHOBOS collaboration [100]. Panel (a) shows centrality classes in the range 0%–25% and panel (b) shows centrality classes in the range 25%–50%.

Turning to collective flow, we now present results for v_2. In all cases, the theoretical result is computed by using the event-plane method. Because we use smooth Glauber initial conditions, we do not compute the higher-order harmonics. In addition, for v_2 we do not expect to reproduce observations in the most-centrality classes since, in such classes, elliptic flow is sensitive to event-by-event fluctuations in the geometry, which are not captured by our initial conditions.

We start with Fig. 7 which shows the elliptic flow for charged particles in four different centrality classes: (a) 0%–10%, (b) 10%–20%, (c) 20%–30%, and (d) 30%–40%. The solid red line is the aHydroQP prediction and the points are observations by the PHENIX collaboration [101]. As can be seen from this figure, aHydroQP (black line) describes reasonably well the observed charged-particle v_2 as a function of transverse momentum given the simplicity of the model. We notice that in the most-centrality class (0%–10%) we are underestimating the magnitude of v_2, but this is to be expected since we have used smooth initial conditions. In the 20%–30% and 30%–40% centrality classes

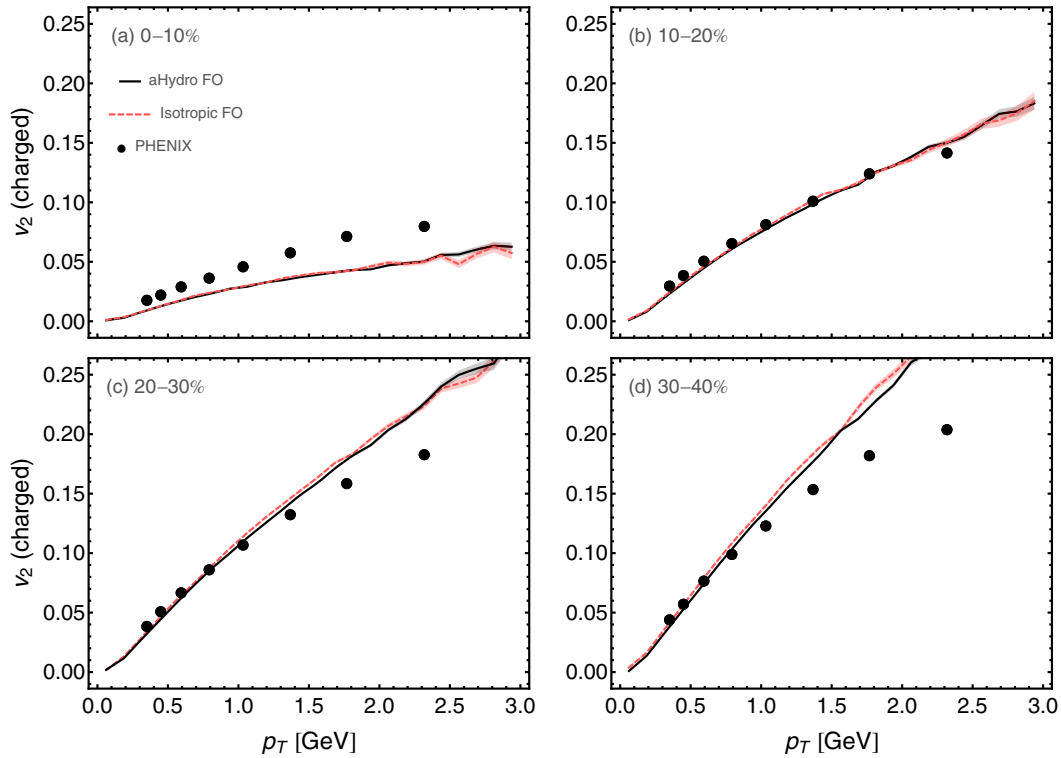

FIG. 7. Elliptic flow for charged particles in four different centrality classes: (a) 0%–10%, (b) 10%–20%, (c) 20%–30%, and (d) 30%–40%. The solid black line is the aHydroQP prediction and the points are observations by the PHENIX collaboration [101]. The experimental errors reported by the PHENIX collaboration are smaller than the point size used. For comparison, the red dashed line shows the result obtained when an isotropic freeze-out prescription with the same effective temperature is used.

(bottom row) we see that aHydroQP overpredicts v_2 at high transverse momentum. In standard viscous hydrodynamics, one sees a larger "downward bending" of v_2 at high p_T due to the viscous correction to the one-particle distribution function [102]; however, such large corrections to one-particle distribution function call into doubt the suitability of using only terms that are linear in the viscous tensor. In aHydroQP, there is no such truncation and terms of infinitely high order in the momentum-space anisotropies are resummed [61]. As a result, aHydroQP predicts a smaller viscous correction to the ideal hydrodynamics result for the distribution function and hence overshoots the data more than standard second-order viscous hydrodynamics treatments do. To illustrate this explicitly, in Fig. 7 we have included a curve (red dashed) showing the charged elliptic flow which results if one ignores the momentum-space anisotropy present on the freeze-out hypersurface (similar to how we studied the effect of momentum-anisotropy on the particle spectra in Fig. 3). As can be seen by comparing the black and red dashed lines in Fig. 7, there is at best only a small effect on the charged particle elliptic flow when comparing anisotropic vs isotropic freeze-out. This stands in stark contrast to the large corrections seen when changing from isotropic to anisotropic freeze-out in the identified particle spectra Fig. 3.

In Fig. 8 we present our results for the identified particle elliptic flow for pions, kaons, and protons as a function of transverse momentum. We compare our model predictions with experimental observations available from the PHENIX collaboration [103]. The blue solid line, red dashed line, and green dotted lines are the aHydroQP predictions for pions, kaons, and protons, respectively. The blue squares, red triangles, and green circles are experimental observations. As can

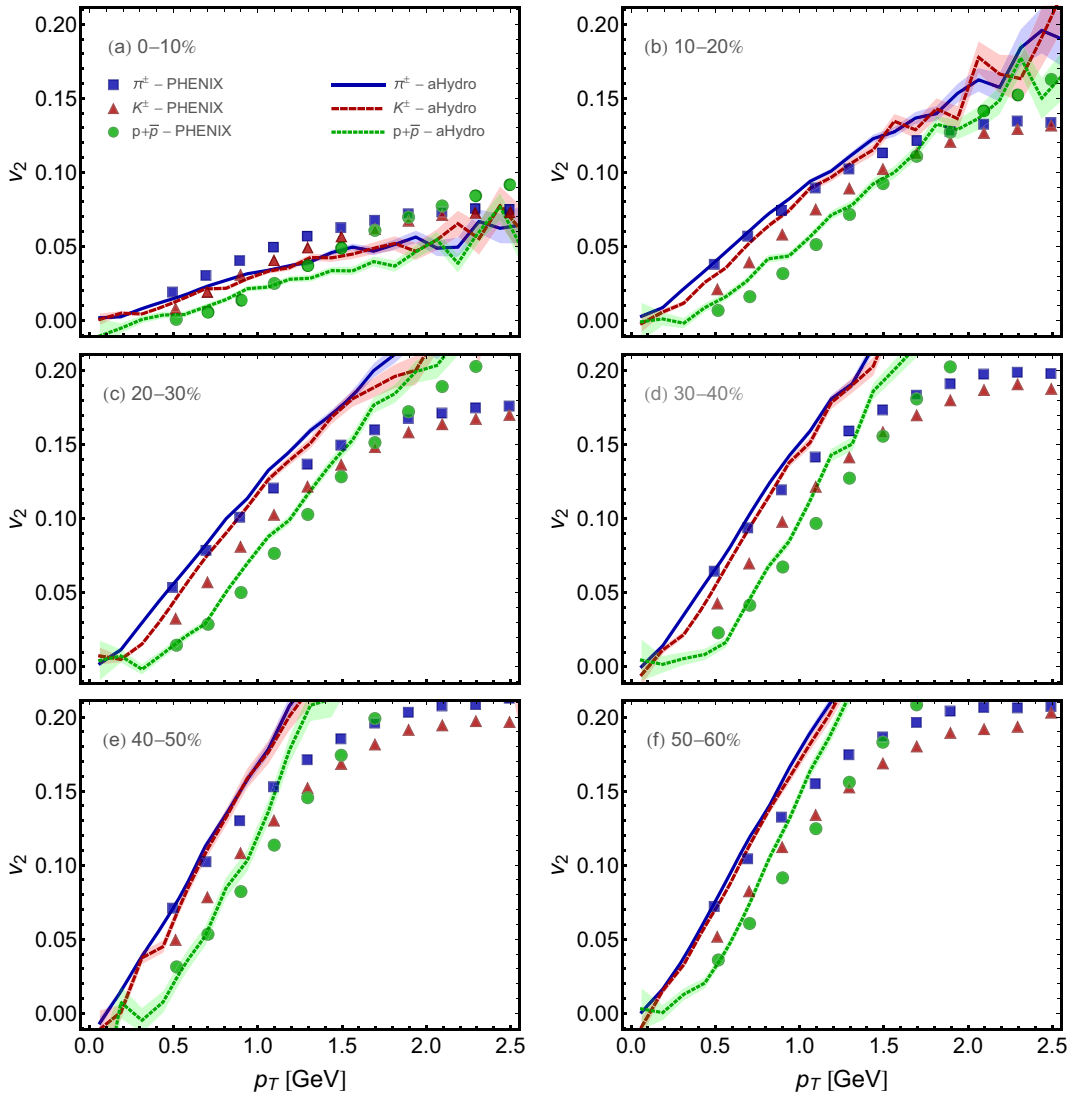

FIG. 8. aHydroQP results for the identified particle elliptic flow as a function of transverse momentum compared with experimental data from the PHENIX collaboration [103]. The blue solid line, red dashed line, and green dotted lines are the aHydroQP predictions for pions, kaons, and protons, respectively. The blue squares, red triangles, and green circles are experimental observations. The panels (a)–(f) show the centrality classes 0%–10%, 10%–20%, 20%–30%, 30%–40%, 40%–50%, and 50%–60%.

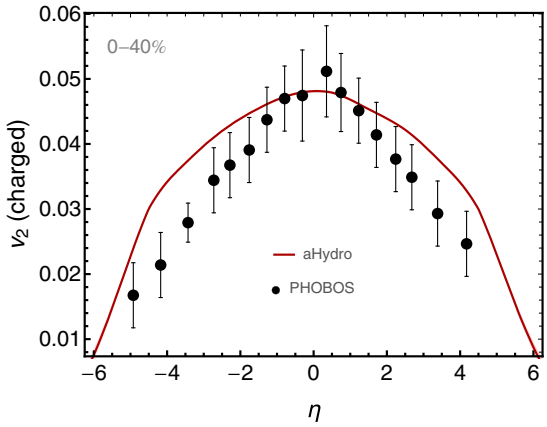

FIG. 9. Comparison between our aHydroQP model results for the integrated elliptic flow versus pseudorapidity and experimental data from the PHOBOS collaboration [104,105]. The aHydroQP results are indicated by a solid red line and the PHOBOS data by black points with error bars. The experimental error bars include both statistical and systematic uncertainties.

be seen from this figure, the mass ordering observed is qualitatively reproduced; however, the agreement with the RHIC data is poorer than what was found when comparing with ALICE data from the LHC 2.76 TeV collisions [76,77]. We also note that, in all cases shown, the kaon elliptic flow is not well reproduced. This is similar to what other modern viscous hydrodynamics codes coupled to hadronic afterburners have found when including bulk viscous effects at RHIC energies [106,107].

Finally, in Fig. 9 we present a comparison between our aHydroQP model results for the integrated elliptic flow versus pseudorapidity and experimental data from the PHOBOS collaboration [104,105]. The aHydroQP results are indicated by a solid red line and the PHOBOS data by black points with error bars. The experimental error bars include both statistical and systematic uncertainties. As can be seen from this figure, aHydroQP does a quite good job in reproducing the overall shape of the elliptic flow versus pseudorapidity; however, the aHydroQP model results have a slightly wider profile than the experimental observations. This should be contrasted with aHydroQP applied to LHC 2.76 TeV energies where it was found that the elliptic flow dropped off too slowly to accurately describe the experimental observations of the ALICE collaboration [77]. Explanations for the discrepancy could include our assumption of a temperature-independent Shear-viscosity-to-entropy-density ratio or event plane decorrelation in the rapidity direction. We plan to investigate these effects in the context of aHydroQP in a forthcoming presentation.

IV. CONCLUSIONS AND OUTLOOK

In this paper we have applied the aHydroQP formalism to phenomenological predictions for a variety of observables measured at RHIC highest beam energies. We presented comparisons of identified particle spectra in different centrality classes, charged particle multiplicity versus pseudorapidity, identified particle multiplicity versus centrality across a wide range of particle species, identified particle elliptic flow versus transverse momentum, and charged particle elliptic flow as a function of transverse momentum and rapidity. We used the same aHydroQP and hadronic production codes that were used previously to describe LHC 2.76 TeV data.

The aHydroQP hydrodynamic model that we used includes effects of both shear and bulk viscosities in addition to an infinite number of transport coefficients computed self-consistently in the relaxation-time approximation. To convert to the final-state hadrons, we used anisotropic Cooper–Frye freeze-out performed on a fixed-energy-density hypersurface and computed the production and feed-down by using a customized version of Therminator 2. We found good agreement with many heavy-ion collision observables by using only smooth Glauber initial conditions parametrized by an initial central temperature of $T_0 = 455$ MeV, a constant shear-viscosity-to-entropy-density ratio $\eta/s = 0.179$, and a switching (freeze-out) temperature of $T_{\rm FO} = 130$ MeV.

Looking forward, the next hurdles on the aHydroQP front are to include the off-diagonal momentum-space anisotropies in the calculation and to produce results with fluctuating initial conditions. In addition, we are currently studying the effects of different parametrizations of the temperature dependence of η/s. The results presented here should provide a baseline for these future works.

ACKNOWLEDGMENTS

D. Almaalol was supported by a fellowship from the University of Zawia, Libya. M. Alqahtani was supported by Imam Abdulrahman Bin Faisal University, Saudi Arabia. M. Strickland was supported by the U.S. Department of Energy, Office of Science, Office of Nuclear Physics under Award No. DE-SC0013470.

[1] P. Huovinen, P. F. Kolb, U. W. Heinz, P. V. Ruuskanen, and S. A. Voloshin, Phys. Lett. B **503**, 58 (2001).
[2] T. Hirano and K. Tsuda, Phys. Rev. C **66**, 054905 (2002).
[3] P. F. Kolb and U. W. Heinz, in *Quark Gluon Plasma 3*, edited by R. C. Hwa and X.-N. Wang (World Scientific, Singapore, 2003), p. 634.
[4] P. F. Kolb, J. Sollfrank, and U. W. Heinz, Phys. Lett. B **459**, 667 (1999).
[5] U. W. Heinz, AIP Conf. Proc. **602**, 281 (2001).
[6] U. W. Heinz and P. F. Kolb, in *Proceedings of the 18th Winter Workshop on Nuclear Dynamics*, edited by R. Bellwied, J. Harris, and W. Bauer (EP Systema, Debrecen, Hungary, 2002), pp. 205–216.
[7] P. Jacobs and X.-N. Wang, Prog. Part. Nucl. Phys. **54**, 443 (2005).
[8] B. Muller and K. Rajagopal, Eur. Phys. J. C **43**, 15 (2005).
[9] M. Strickland, J. Phys. G **34**, S429 (2007).
[10] R. Ryblewski, J. Phys. G **40**, 093101 (2013).

[11] M. Strickland, Acta Phys. Pol., B **45**, 2355 (2014).
[12] M. Alqahtani, M. Nopoush, and M. Strickland, Prog. Part. Nucl. Phys. **101**, 204 (2018).
[13] I. Muller, Eur. Phys. J. A **198**, 329 (1967).
[14] W. Israel, Ann. Phys. (NY) **100**, 310 (1976).
[15] W. Israel and J. M. Stewart, Ann. Phys. (NY) **118**, 341 (1979).
[16] A. Muronga, Phys. Rev. Lett. **88**, 062302 (2002).
[17] A. Muronga, Phys. Rev. C **69**, 034903 (2004).
[18] A. Muronga and D. H. Rischke, arXiv:nucl-th.0407114.
[19] U. W. Heinz, H. Song, and A. K. Chaudhuri, Phys. Rev. C **73**, 034904 (2006).
[20] R. Baier, P. Romatschke, and U. A. Wiedemann, Phys. Rev. C **73**, 064903 (2006).
[21] P. Romatschke and U. Romatschke, Phys. Rev. Lett. **99**, 172301 (2007).
[22] R. Baier, P. Romatschke, D. T. Son, A. O. Starinets, and M. A. Stephanov, J. High Energy Phys. 04 (2008) 100.
[23] K. Dusling and D. Teaney, Phys. Rev. C **77**, 034905 (2008).
[24] M. Luzum and P. Romatschke, Phys. Rev. C **78**, 034915 (2008).
[25] H. Song and U. W. Heinz, J. Phys. G **36**, 064033 (2009).
[26] U. W. Heinz, *Relativistic Heavy Ion Physics, Landolt-Boernstein New Series, I/23*, edited by R. Stock (Springer Verlag, New York, 2010), Chap. 5.
[27] A. El, Z. Xu, and C. Greiner, Phys. Rev. C **81**, 041901 (2010).
[28] J. Peralta-Ramos and E. Calzetta, Phys. Rev. D **80**, 126002 (2009).
[29] J. Peralta-Ramos and E. Calzetta, Phys. Rev. C **82**, 054905 (2010).
[30] G. Denicol, T. Kodama, and T. Koide, J. Phys. G **37**, 094040 (2010).
[31] G. S. Denicol, T. Koide, and D. H. Rischke, Phys. Rev. Lett. **105**, 162501 (2010).
[32] B. Schenke, S. Jeon, and C. Gale, Phys. Rev. Lett. **106**, 042301 (2011).
[33] B. Schenke, S. Jeon, and C. Gale, Phys. Lett. B **702**, 59 (2011).
[34] P. Bozek, Phys. Lett. B **699**, 283 (2011).
[35] H. Niemi, G. S. Denicol, P. Huovinen, E. Molnár, and D. H. Rischke, Phys. Rev. Lett. **106**, 212302 (2011).
[36] G. S. Denicol, J. Noronha, H. Niemi, and D. H. Rischke, Phys. Rev. D **83**, 074019 (2011).
[37] H. Niemi, G. S. Denicol, P. Huovinen, E. Molnár, and D. H. Rischke, Phys. Rev. C **86**, 014909 (2012).
[38] P. Bożek and I. Wyskiel-Piekarska, Phys. Rev. C **85**, 064915 (2012).
[39] G. S. Denicol, H. Niemi, E. Molnár, and D. H. Rischke, Phys. Rev. D **85**, 114047 (2012).
[40] G. Denicol, E. Molnár, H. Niemi, and D. Rischke, Eur. Phys. J. A **48**, 170 (2012).
[41] J. Peralta-Ramos and E. Calzetta, Phys. Rev. D **87**, 034003 (2013).
[42] A. Jaiswal, Phys. Rev. C **87**, 051901 (2013).
[43] A. Jaiswal, Phys. Rev. C **88**, 021903 (2013).
[44] E. Calzetta, Phys. Rev. D **92**, 045035 (2015).
[45] G. S. Denicol, S. Jeon, and C. Gale, Phys. Rev. C **90**, 024912 (2014).
[46] G. S. Denicol, W. Florkowski, R. Ryblewski, and M. Strickland, Phys. Rev. C **90**, 044905 (2014).
[47] A. Jaiswal, R. Ryblewski, and M. Strickland, Phys. Rev. C **90**, 044908 (2014).
[48] S. Jeon and U. Heinz, in *Quark-Gluon Plasma 5*, edited by X.-N. Wang (World Scientific, Singapore, 2016), pp. 131–187.
[49] P. Romatschke and U. Romatschke, arXiv:1712.05815.
[50] W. Florkowski, M. P. Heller, and M. Spalinski, Rep. Prog. Phys. **81**, 046001 (2018).
[51] W. Florkowski and R. Ryblewski, Phys. Rev. C **83**, 034907 (2011).
[52] M. Martinez and M. Strickland, Nucl. Phys. A **848**, 183 (2010).
[53] W. Florkowski, R. Ryblewski, and M. Strickland, Nucl. Phys. A **916**, 249 (2013).
[54] W. Florkowski, R. Ryblewski, and M. Strickland, Phys. Rev. C **88**, 024903 (2013).
[55] W. Florkowski, E. Maksymiuk, R. Ryblewski, and M. Strickland, Phys. Rev. C **89**, 054908 (2014).
[56] M. Nopoush, R. Ryblewski, and M. Strickland, Phys. Rev. C **90**, 014908 (2014).
[57] G. S. Denicol, U. W. Heinz, M. Martinez, J. Noronha, and M. Strickland, Phys. Rev. Lett. **113**, 202301 (2014).
[58] G. S. Denicol, U. W. Heinz, M. Martinez, J. Noronha, and M. Strickland, Phys. Rev. D **90**, 125026 (2014).
[59] U. Heinz, D. Bazow, G. S. Denicol, M. Martinez, M. Nopoush, J. Noronha, R. Ryblewski, and M. Strickland, Nucl. Part. Phys. Proc. **276–278**, 193 (2016).
[60] E. Molnar, H. Niemi, and D. H. Rischke, Phys. Rev. D **94**, 125003 (2016).
[61] M. Strickland, J. Noronha, and G. S. Denicol, Phys. Rev. D **97**, 036020 (2018).
[62] R. Ryblewski and W. Florkowski, Acta Phys. Pol., B **42**, 115 (2011).
[63] W. Florkowski and R. Ryblewski, Phys. Rev. C **85**, 044902 (2012).
[64] M. Martinez, R. Ryblewski, and M. Strickland, Phys. Rev. C **85**, 064913 (2012).
[65] R. Ryblewski and W. Florkowski, Phys. Rev. C **85**, 064901 (2012).
[66] D. Bazow, U. W. Heinz, and M. Strickland, Phys. Rev. C **90**, 054910 (2014).
[67] L. Tinti and W. Florkowski, Phys. Rev. C **89**, 034907 (2014).
[68] L. Tinti, Phys. Rev. C **94**, 044902 (2016).
[69] D. Bazow, U. W. Heinz, and M. Martinez, Phys. Rev. C **91**, 064903 (2015).
[70] M. Strickland, M. Nopoush, and R. Ryblewski, Nucl. Phys. A **956**, 268 (2016).
[71] M. Alqahtani, M. Nopoush, and M. Strickland, Phys. Rev. C **92**, 054910 (2015).
[72] E. Molnar, H. Niemi, and D. H. Rischke, Phys. Rev. D **93**, 114025 (2016).
[73] M. Alqahtani, M. Nopoush, and M. Strickland, Phys. Rev. C **95**, 034906 (2017).
[74] M. Bluhm and T. Schäfer, Phys. Rev. A **92**, 043602 (2015).
[75] M. Bluhm and T. Schäfer, Phys. Rev. Lett. **116**, 115301 (2016).
[76] M. Alqahtani, M. Nopoush, R. Ryblewski, and M. Strickland, Phys. Rev. Lett. **119**, 042301 (2017).
[77] M. Alqahtani, M. Nopoush, R. Ryblewski, and M. Strickland, Phys. Rev. C **96**, 044910 (2017).
[78] M. Martinez, M. McNelis, and U. Heinz, Phys. Rev. C **95**, 054907 (2017).
[79] M. McNelis, D. Bazow, and U. Heinz, Phys. Rev. C **97**, 054912 (2018).

[80] M. Strickland, Phys. Rev. Lett. **107**, 132301 (2011).
[81] M. Strickland and D. Bazow, Nucl. Phys. A **879**, 25 (2012).
[82] B. Krouppa, R. Ryblewski, and M. Strickland, Phys. Rev. C **92**, 061901 (2015).
[83] B. Krouppa and M. Strickland, Universe **2**, 16 (2016).
[84] B. Krouppa, R. Ryblewski, and M. Strickland, Nucl. Phys. A **967**, 604 (2017).
[85] B. Krouppa, A. Rothkopf, and M. Strickland, Phys. Rev. D **97**, 016017 (2018).
[86] P. Romatschke and M. Strickland, Phys. Rev. D **68**, 036004 (2003).
[87] P. Romatschke and M. Strickland, Phys. Rev. D **70**, 116006 (2004).
[88] S. Jeon and L. G. Yaffe, Phys. Rev. D **53**, 5799 (1996).
[89] P. Romatschke, Phys. Rev. D **85**, 065012 (2012).
[90] S. A. Bass, J. E. Bernhard, and J. S. Moreland, Nucl. Phys. A **967**, 67 (2017).
[91] R. Rougemont, R. Critelli, J. Noronha-Hostler, J. Noronha, and C. Ratti, Phys. Rev. D **96**, 014032 (2017).
[92] S. Ryu, J. F. Paquet, C. Shen, G. S. Denicol, B. Schenke, S. Jeon, and C. Gale, Phys. Rev. Lett. **115**, 132301 (2015).
[93] M. Nopoush, M. Strickland, R. Ryblewski, D. Bazow, U. Heinz, and M. Martinez, Phys. Rev. C **92**, 044912 (2015).
[94] M. Chojnacki, A. Kisiel, W. Florkowski, and W. Broniowski, Comput. Phys. Commun. **183**, 746 (2012).
[95] aHydro Collaboration, http://personal.kent.edu/~mstrick6/code/ (2015).
[96] P. Bozek and I. Wyskiel, Phys. Rev. C **81**, 054902 (2010).
[97] S. S. Adler *et al.* (PHENIX Collaboration), Phys. Rev. C **69**, 034909 (2004).
[98] J. Adams *et al.* (STAR Collaboration), Phys. Lett. B **612**, 181 (2005).
[99] J. Adams *et al.* (STAR Collaboration), Phys. Rev. Lett. **98**, 062301 (2007).
[100] B. Alver *et al.* (PHOBOS Collaboration), Phys. Rev. C **83**, 024913 (2011).
[101] A. Adare *et al.* (PHENIX Collaboration), Phys. Rev. Lett. **98**, 162301 (2007).
[102] D. Teaney, Phys. Rev. C **68**, 034913 (2003).
[103] A. Adare *et al.* (PHENIX Collaboration), Phys. Rev. C **93**, 051902 (2016).
[104] B. B. Back *et al.* (PHOBOS Collaboration), Phys. Rev. Lett. **94**, 122303 (2005).
[105] B. B. Back *et al.* (PHOBOS Collaboration), Phys. Rev. C **72**, 051901 (2005).
[106] S. Ryu, J.-F. Paquet, C. Shen, G. Denicol, B. Schenke, S. Jeon, and C. Gale, Phys. Rev. C **97**, 034910 (2018).
[107] H. Petersen, https://indico.cern.ch/event/656452/contributions/2869811/ (2018).